

A redshift-independent theoretical halo mass function validated with the Uchuu simulations

Elena Fernández-García¹, Juan E. Betancort-Rijo^{2,3}, Francisco Prada¹, Tomoaki Ishiyama⁴, Anatoly Klypin⁵, and José Ruedas¹

¹ Instituto de Astrofísica de Andalucía (CSIC), E18008 Granada, Spain,

² Instituto de Astrofísica de Canarias, C/ Via Lactea s/n, Tenerife E38200, Spain

³ Facultad de Física, Universidad de La Laguna, Astrofísico Francisco Sanchez, s/n, La Laguna, Tenerife E38200, Spain

⁴ Digital Transformation Enhancement Council, Chiba University, 1-33, Yayoi-cho, Inage-ku, Chiba, 263-8522, Japan

⁵ Department of Astronomy, University of Virginia, Charlottesville, VA 22904, USA

Received ..., ...; accepted ..., ...

ABSTRACT

We present a new theoretical framework for the halo mass function (HMF) that accurately predicts the abundance of dark matter haloes across an exceptionally wide range in mass and redshift. Building on a generalised Press & Schechter model and triaxial collapse (GPS+), we predict the HMF in terms of the variance of the linear density field, with only a weak explicit dependence on halo mass and no explicit dependence on redshift. The GPS+ model naturally provides the correct normalization and high-mass behaviour without requiring empirical fitting. We calibrate and validate the GPS+ model using the Uchuu *N*-body simulation suite, which combines large cosmological volume and high mass resolution under *Planck* cosmology. Using six simulations with up to 300 realizations, we obtain precision HMF measurements spanning halo masses in the range $6.5 \leq \log(M_{200m}/[h^{-1}M_{\odot}]) \leq 16$ over $0 \leq z \leq 20$, with reduced cosmic variance. Across this full domain, the GPS+ model reproduces the simulated HMF with deviations typically below 10–20%. Comparison with the Sheth–Tormen (ST) model shows similar performance at $z \lesssim 2$, but markedly improved agreement at higher redshifts, where ST can deviate by 70–80% while our model remains within $\sim 20\%$. Finally, we assess the impact of the halo mass definition: adopting the evolving virial overdensity of Bryan & Norman (1998) worsens agreement at low redshift and high masses, whereas M_{200m} yields a more universal, nearly redshift-independent HMF.

Key words. cosmology, dark matter, halos, theory, large-scale structure

1. Introduction

The halo mass function (HMF), which measures the abundance of dark matter halos as a function of mass, is a cornerstone of cosmology. It encodes the growth of structure from the early Universe to the present and is a key tool for constraining cosmological models and parameters (Cooray & Sheth 2002; Mo et al. 2010; Castro et al. 2016). Reliable predictions of its mass and redshift dependence are essential for interpreting observations from large-scale structure galaxy surveys.

The theoretical framework of the HMF was originally developed by Press & Schechter (1974) through the Press–Schechter (PS, hereafter) formalism, later extended with excursion set theory (Bond et al. 1991; Lacey & Cole 1993) and refined with ellipsoidal collapse models (Sheth & Tormen 1999; Sheth et al. 2001, hereafter ST). Empirical calibrations based on *N*-body simulations (e.g. Jenkins et al. 2001; Tinker et al. 2008; Despali et al. 2016; Shirasaki et al. 2021; Seppi et al. 2021) have since improved the accuracy of HMF predictions across a range of cosmologies, halo masses and redshifts. However, each proposed fitting formula remains limited to a specific dynamical range. For example, the calibrations of Jenkins et al. (2001) and Reed et al. (2003) apply primarily to cluster-scale halos at $z \lesssim 3$, while those of Tinker et al. (2008) and Despali et al. (2016) extend toward higher redshift but are still restricted to $z \lesssim 10$ and halo masses typically above $10^{10} h^{-1} M_{\odot}$. Even more recent high-redshift cali-

brations (Seppi et al. 2021) do not reach the dwarf-galaxy regime nor extend beyond $z \sim 2$. Consequently, no existing model provides a fully self-consistent description of the HMF spanning the full cosmic history and the complete hierarchy of halo masses. The advent of state-of-the-art numerical experiments such as the Uchuu *N*-body simulation suite (Ishiyama et al. 2021; Ishiyama et al. in prep.), with its unprecedented combination of volume and mass resolution, now enables precision HMF measurements across a much wider domain in both mass and redshift, addressing these longstanding limitations.

In this work, we revisit the generalised Press–Schechter approach introduced by Betancort-Rijo & Montero-Dorta (2006b,a) and present a new formulation that delivers a consistent description of the halo mass function (HMF) from dwarf-scale halos up to the most massive clusters, with halo masses in the range $6.5 < \log(M/M_{\odot}) < 16$, spanning from the present epoch ($z = 0$) to the early universe ($z \sim 20$). Although the generalised Press–Schechter framework is a fundamental component of our methodology, it is not the only one: the triaxial collapse plays an essential role in the development of our formalism. We refer to the entire framework as “GPS+” throughout this work. In this predominantly theoretical setting, with only minimal parameter fitting to the Uchuu simulation suite, the mass function depends primarily on root mean square of density fluctuations, $\sigma(M, z)$, with only a weak explicit dependence on M and no explicit dependence on redshift z . This unprecedented dynamical range is made possible by the Uchuu suite of *N*-body simula-

* e-mail: efdez@iaa.es

tions, which for the first time provide coverage across such an extensive domain in halo mass and redshift. By calibrating the model over multiple simulation snapshots, we achieve percent-level accuracy across this broad parameter space. These results establish a robust theoretical foundation for interpreting data from upcoming and ongoing galaxy and cluster surveys such as DESI (DESI Collaboration 2025), Euclid (Laureijs et al. 2011), Subaru PFS (Takada et al. 2014), LSST (Ivezić et al. 2019) and eROSITA (Ghirardini et al. 2024), as well as observations of early galaxies with the James Webb Space Telescope (McElwain et al. 2023).

Although the framework developed in this work is rooted in the classical PS picture, it replaces the original collapse-assignment criterion with a more physically motivated one. The approach remains within the same conceptual domain and does not extend the scope of PS; rather, it offers a modified formulation that better captures the physics of halo formation while preserving the fundamental statistical properties of Gaussian random fields.

In Section 2 we present the suite of the UCHUU simulations used in this work and present the HMF measured in these simulations. In Section 3 we present the theoretical framework that predicts the HMF for a wide range of redshifts, with no explicit dependence on the redshift. In Section 4 we show the performance of this theoretical framework compared to the results predicted by the UCHUU simulations presented in Section 2. Finally, in Section 5, we summarise the main results obtained in this work.

2. Uchuu simulations

In this work, we use the suite of UCHUU simulations with different mass resolutions to test the theoretical framework presented here. The simulations employed are: PHI-4096, SHIN-UCHUU, UCHUU, MUCHO-UCHUU-140M, MUCHO-UCHUU-1G and MUCHO-UCHUU-6G[§], described in Ishiyama et al. (2021) and Ishiyama et al. (in prep.). The main properties are summarized in Table 1. The first three simulations adopt the Planck15 cosmology (Planck Collaboration 2016) ($\Omega_m = 0.3089, \Omega_\Lambda = 0.6911, h = 0.6774, \sigma_8 = 0.8159, \Omega_b = 0.0486, n_s = 0.9667$), whereas the remaining three follow the Planck18 parameters (Planck Collaboration 2020) ($\Omega_m = 0.3111, \Omega_\Lambda = 0.6889, h = 0.6766, \sigma_8 = 0.8102, \Omega_b = 0.048975, n_s = 0.9665$). Although the cosmologies differ slightly, the impact on the resulting HMF is small and negligible compared to both the intrinsic uncertainties in the simulated mass functions and those arising from the theoretical model itself.

For MUCHO-UCHUU-140M, we use 50 independent realizations, 300 realizations for MUCHO-UCHUU-1G, and 100 realisations for MUCHO-UCHUU-6G. This ensemble approach is crucial, as the final HMF is obtained by averaging over all realizations and estimating uncertainties from the diagonal of the covariance matrix. As a result, the contribution from cosmic variance is significantly reduced. As a curiosity, in the total volume of $600 \text{ Gpc}^3/h^3$ of the 100 MUCHO-UCHUU-6G realizations, the most massive halo found has a mass of $8.3 \times 10^{15} M_\odot$, which is about 13 times larger than the Virgo cluster (Kashibadze et al. 2020).

All simulations were generated using the *TreePM* code *Greem*^{*} (Ishiyama et al. 2009; Ishiyama et al. 2012). PHI-4096, SHIN-UCHUU and UCHUU were run on the ATERUI II supercomputer at Center for Computational Astrophysics, CfCA,

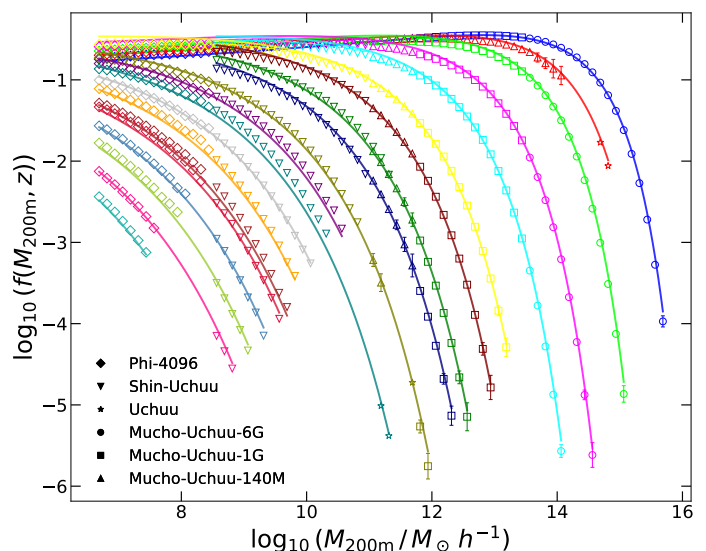


Fig. 1: The markers show the measurements of the multiplicity function, $f(M, z)$ (see Equation 1), obtained from the suite of UCHUU simulations at different redshifts. The solid lines correspond to the predictions from the multiplicity function from the GPS+ model at each redshift. Each colour represents a different redshift, ranging from $z = 0$ to $z = 20$ from right to left (see Table A.2 for the full list). The y-axis shows the normalized differential halo abundance, including the derivative term $d \ln M / d \ln \sigma$. For the measurements, we only include mass bins containing more than 200 halos.

National Astronomical Observatory of Japan, while the MUCHO-UCHUU simulations were carried out on the FUGAKU supercomputer at the Riken Center for Computational Science in Kobe, Japan. Halos were identified using the *RockStar* halo/subhalo finder[†] (Behroozi et al. 2013a) and its distributed extension *MPI-Rockstar*[‡] (Tokuue et al. 2024), and merger trees were constructed using the *Consistent Trees* code (Behroozi et al. 2013b).

Figure 1 shows the combined HMF derived from all the simulations used in this work. We express it in terms of the multiplicity function (e.g. Sheth & Tormen 1999), defined as:

$$f(M, z) = \log_{10} \left(\frac{M_{200m}}{\rho_m} \frac{dn}{d \ln M_{200m}} \left| \frac{d \ln M_{200m}}{d \ln \sigma} \right| \right). \quad (1)$$

We adopt the halo mass defined as the mass enclosed within overdensity of $200\rho_b$, denoted M_{200m} , where ρ_b is the mean background matter density of the Universe. Unlike the virial mass, this definition does not depend on redshift, as the overdensity threshold remains fixed rather than evolving with cosmology. A detailed justification for this choice is provided in Appendix C.

To construct the combined HMF at each redshift, we require a minimum of 407 particles per halo in all simulation to ensure completeness at the low-mass end. At the high-mass end of each, the HMF from each simulation is limited to guarantee a smooth and continuous transition across the overlapping mass ranges of the different simulations. The resulting HMFs from all simulations are provided as electronic tables, as described in Appendix A.

[§]All simulations are publicly available at <https://skiesanduniverses.org/Simulations/Uchuu/>

^{*}<http://hpc.imit.chiba-u.jp/~ishiytm/greem/>

[†]<https://bitbucket.org/gfcstanford/rockstar/>

[‡]<https://github.com/Tomoaki-Ishiyama/mpi-rockstar/>

Name	N	L [Mpc/h]	$M_p [M_\odot/h]$	$\varepsilon [h^{-1}\text{kpc}]$	#	Cosmology	Ref.
Phi-4096	4096 ³	16	5.13×10^3	0.06	1	Planck15	Ishiyama et al. (2021)
Shin-Uchuu	6400 ³	140	8.96×10^5	0.4	1	Planck15	Ishiyama et al. (2021)
Uchuu	12800 ³	2000	3.27×10^8	4.27	1	Planck15	Ishiyama et al. (2021)
Mucho-Uchuu-140M	1024 ³	140	2.21×10^8	3.75	50	Planck18	Ishiyama et al. (in prep.)
Mucho-Uchuu-1G	4096 ³	1000	1.26×10^9	8	300	Planck18	Ishiyama et al. (in prep.)
Mucho-Uchuu-6G	6144 ³	6000	8.04×10^{10}	16	100	Planck18	Ishiyama et al. (in prep.)

Table 1: The number of dark matter particles used in each simulation, the box size (L_{box}), the dark matter particle mass (M_{part}), the gravitational softening length (ε), the number of realizations (#), and the adopted cosmological parameters.

3. Theoretical framework

We model the HMF using a GPS+ framework capable of describing the abundance of halos over an exceptionally wide mass range ($\log M/[h^{-1}M_\odot] \sim 6.5\text{--}16.0$) and up to very high redshifts ($z \sim 20$). The starting point of the formalism remains the basic PS idea that a mass element belongs to a halo of mass M if an associated smoothed density field satisfies a collapse condition. Our formulation, however, replaces the original centre-based criterion with a physically more realistic one, while still relying on the same statistical properties of Gaussian fields that underlie both PS and excursion-set arguments. It also incorporates the physics of the triaxial collapse. In this sense, the method retains the conceptual structure of PS but modifies the criteria for assigning a mass element to a collapsed object with mass larger than M .

In this framework, the HMF is written as:

$$\frac{dn(M, z)}{dM} = \frac{\rho_m}{M} \frac{dF(M, z)}{dM}, \quad (2)$$

where ρ_m is the matter density, and $F(M, z)$ is the mass fraction.

The mass fraction is defined as:

$$F(M) = \frac{\text{erfc}[\langle \delta_c(\sigma(M, z), M) \rangle / (\sqrt{2} \sigma(M, z))]}{V(\Sigma(M, z), M)}, \quad (3)$$

with $V(\Sigma(M, z), M)$ (see Appendix B for an explanation) given by:

$$V(\Sigma(M, z), M) = 3 \int_0^1 \text{erfc} \left[\frac{\langle \delta_c \rangle (\sigma(M, z), M)}{\sqrt{2} \Sigma(M, z)} \right] \times \sqrt{\frac{1 - \exp(-c(M) \xi^2)}{1 + \exp(-c(M) \xi^2)}} \xi^2 d\xi \quad (4)$$

where δ_l encodes the linear growth corrections at $z = 0$, $\Sigma(M, z)$ is given by

$$\Sigma(M, z) = \sqrt{\sigma^2(M, z) + U^2(\sigma/\delta_c)}, \quad (5)$$

where $\sigma(M, z)$ is the standard linear-theory variance, and the correction function $U(x)$ is defined as:

$$U(x) = -0.01507 + 0.17810 \cdot x + 0.03835 \cdot x^2 - 0.00221 \cdot x^3, \quad (6)$$

where $x = \sigma(M, z)/\delta_c$, and δ_c is the critical overdensity, equal to the linear-theory density contrast δ_l in the spherical-collapse approximation at collapse. In our model, the critical overdensity

for collapse is further modified as a function of mass and redshift:

$$\langle \delta_c \rangle (\sigma(M, z), M) = \delta_c \cdot \left(1 + 0.845 \cdot x - 0.04 \cdot x^2 + 0.0025 \cdot x^3 \right)^B \times A \cdot \left(1 + 0.17 \cdot b(M) - 0.087 \cdot b^2(M) \right)^D, \quad (7)$$

where $b(M)$ is defined by the following polynomial:

$$\log b(x) = -1.28 + 0.05781 \cdot x - 0.005622 \cdot x^2 - 0.0005884 \cdot x^3 - 1.365 \times 10^{-5} \cdot x^4, \quad (8)$$

where $x = \log M$, and A and B are free parameters fitted to the simulation data (see values below), while D is a parameter whose theoretical value is 1 (see Betancort-Rijo et al. in prep.), but we allow to vary in order to test the robustness of this prediction.

Equation 7 comes basically from the physics of the triaxial collapse (see Appendix B for the details).

The function $c(M)$ from Equation 4 is a polynomial defined as:

$$\log c(x) = -1.124 + 0.01756 \cdot x + 0.002539 \cdot x^2 - 6.438 \times 10^{-5} \cdot x^3 + 4.726 \times 10^{-6} \cdot x^4, \quad (9)$$

where $x = \log M$.

This formulation enables the computation of the HMF across a broad halo mass range and out to very high redshifts. A concise overview of the theoretical framework is provided in Appendix B, while a full derivation of the equations will be presented in Betancort-Rijo et al. (in prep.).

The coefficients A and B from Equation 7 were obtained by fitting Equation 2 to the data using the statistic \mathcal{U}^2 , defined as:

$$\mathcal{U}^2 = \sum_{i,j} \frac{|n_{\text{sim}}(M_i, z_j) - n_{\text{th}}(M_i, z_j)|}{n_{\text{sim}}(M_i, z_j)^2} \left[1 - \Theta \left(\frac{\Delta n_{\text{sim}}(M_i, z_j)}{0.05 n_{\text{sim}}(M_i, z_j)} - 1 \right) \right] \quad (10)$$

where $n_{\text{sim}}(M_i, z_j)$ is the HMF measured from the simulations for each halo mass bin M_i and at redshift z_j , $\Delta n_{\text{sim}}(M_i, z_j)$ is the corresponding statistical uncertainty, and $n_{\text{th}}(M_i, z_j)$ is the HMF predicted by the theoretical framework presented in this work. The function Θ is the Heaviside step function, used here to include only those bins with a relative uncertainty smaller than 5%.

It is important to note that the statistical uncertainties were estimated differently for each set of simulations. For Phi-4096,

SHIN-UCHUU and UCHUU, where only a single realisation is available, the uncertainties for each mass bin are assumed to be Poissonian. In contrast, for MUCHO-UCHUU-140M, MUCHO-UCHUU-1G, and MUCHO-UCHUU-6G, we compute uncertainties from the diagonal elements of the covariance matrix constructed using all available realizations.

With this statistic, the best-fitting values obtained for the coefficients A and B are 1.089 and 0.652, respectively. For the parameter D , we explored a range of values and found that the optimal agreement with the simulations results is achieved for D very close to its theoretical value, $D = 1$. This consistency confirms and supports the theoretical prediction.

A key feature of this formalism is that $f(\sigma)$ depends not only on σ but also explicitly on mass through the functions $b(m)$ and $c(m)$ (Equations 8 and 9), while having no explicit dependence on redshift. However, if one neglects this mass dependence and (incorrectly) assumes that $f(\sigma)$ depends solely on σ , one obtains:

$$f(m, z) = f(\sigma(m, z), m) = f(\sigma, m(\sigma, z)) = f(\sigma, z). \quad (11)$$

The first equality is correct: the dependence of $f(\sigma)$ on redshift at a fixed mass arises solely through the term $\sigma(m, z)$. The second equality, however, represents what occurs when the explicit mass dependence of f (at fixed σ) - a key feature of our framework but absent in other formalisms - is artificially removed. By using the $m - \sigma$ relation at fixed redshift, this mass dependence is incorrectly absorbed into an additional (spurious) dependence on σ and an equally spurious dependence on z . This procedure is what leads to the behaviour shown in Figure 2, where $f(\sigma, z)$ appears to vary by nearly 50% across the redshift range considered.

In our formalism, f depends explicitly on both σ and m . The artificial redshift dependence arises only when one forces f to depend on mass exclusively through σ - that is, when adopting the second equality. The resulting $\sim 50\%$ variation is approximately four times larger than the typical modelling uncertainty in the (slightly simplified) form of the framework used here. Since this behaviour depends crucially on the explicit mass dependence predicted by the theory, we regard the trend shown in Figure 2 as strong support for the theoretical foundation of our formalism.

4. Performance of the theoretical framework and comparison with the Sheth & Tormen HMF

In this section, we present the HMF results obtained from the theoretical framework developed and calibrated in this work, along with a comparison to the simulations described previously. For context, we also include a comparison with the widely used ST model. Additional comparisons with other published prescriptions will be presented in Ishiyama et al. (in prep.).

Figure 3 shows the performance of the GPS+ model, where we plot the ratio between the simulated HMF and the prediction from the GPS+ model (black line) across a wide range of redshifts. At low redshifts ($z \leq 2.03$), the ratio remains close to unity over most of the mass range, with deviations of up to $\sim 20\%$ only at the high-mass end ($\log_{10}(M_{200m}/M_{\odot}h^{-1}) > 14$). At $z = 4.27$, we observe a similar $\sim 20\%$ deviation at the low-mass end ($\log_{10}(M_{200m}/M_{\odot}h^{-1}) < 11$). For higher redshifts, the agreement improves further, with deviations typically remaining below 10% across nearly the entire halo mass range. This consistent level of accuracy over such an extended range in mass and

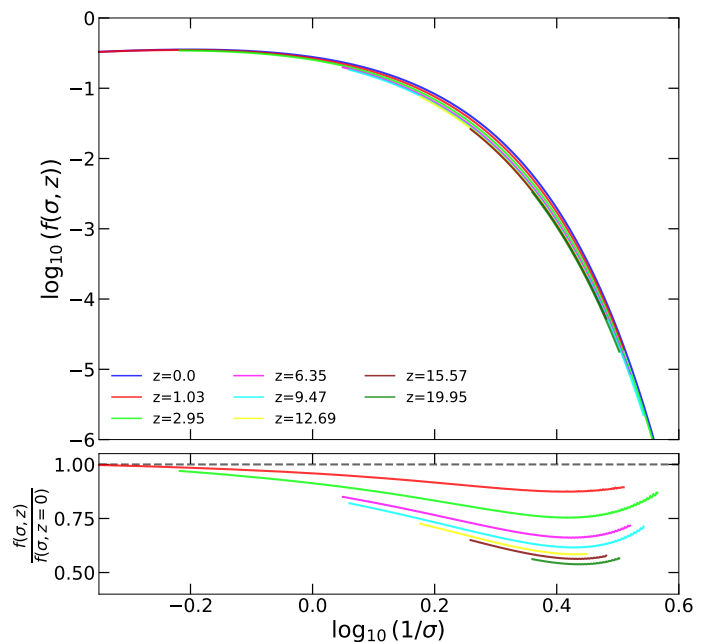


Fig. 2: The top panel shows the multiplicity function $f(\sigma, z)$ as a function of σ at different redshifts, as predicted by the GPS+ model presented in this work. The bottom panel shows the ratio of the model at each redshift to $z = 0$ prediction.

redshift demonstrates the robustness and predictive power of the proposed GPS+ model.

The ST model*, which extends the PS formalism by incorporating ellipsoidal collapse, introduces an explicit dependence on the linear growth factor and therefore allows the HMF to evolve with redshift. In the intermediate redshift range ($0 \lesssim z \lesssim 2$), both the ST prescription and the GPS+ model performs similarly in reproducing the HMF, as shown in Figure 3. However, at higher redshifts ($z \gtrsim 2$), our approach provides a more accurate description, particularly for the most massive halos. This difference becomes increasingly pronounced toward the highest redshifts. For example, at $z \simeq 18.37$, the ST model exhibits deviations of $\sim 60\text{--}80\%$, whereas our framework maintains much smaller discrepancies, typically within $\sim 10\text{--}20\%$. These results demonstrate the robustness of our formalism across a wide halo mass and redshift range and highlight the limitations of other models in the literature when extrapolated to the high-redshift regime.

5. Summary

In this work, we present a theoretical model based on a generalised Press–Shechter with model and triaxial collapse (GPS+), a new theoretical framework that accurately reproduces the HMF across the suite of UCHUU cosmological N -body simulations which span a range of mass resolutions and volumes within the *Planck* cosmology. The framework is physically grounded in the PS picture, but incorporates a modified criterion for assigning a mass element to a collapsed object with mass larger than M , as detailed in the Appendices.

Unlike many previous models, the GPS+ model introduces no explicit redshift dependence; instead the evolution enters

*It is important to note that the ST-model adopts a friend-of-friend mass definition, whereas in this work we use M_{200m} . Therefore, comparisons between the two must be interpreted with this difference in mind.

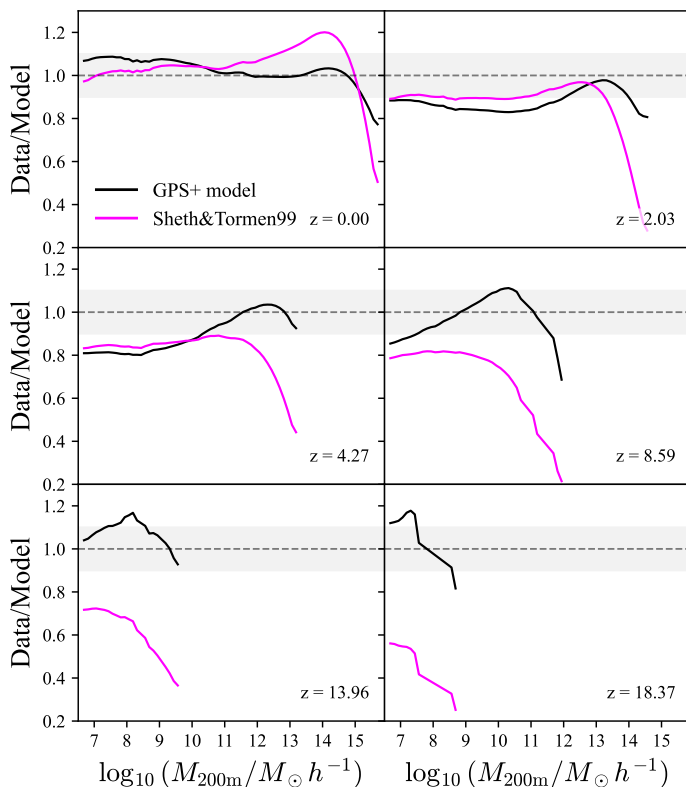


Fig. 3: Ratios between the combined simulated HMF and the predictions from GPS+ model (black line), as well as from the ST model (magenta line) computed using the COLLOSSUS tool (Diemer 2018), at different redshifts. Only mass bins containing more than 100 halos are shown.

solely through the variance of the linear density field, $\sigma(M, z)$. With this formulation, we are able to predict the HMF up to $z \sim 20$ over a halo mass range spanning $\log M_h \sim 6.5$ to $\log M_h \sim 16$.

Across the full mass and redshift range, the GPS+ model achieves deviations typically below 10 – 20%, with the largest differences occurring at the high-mass end of the HMF. We also compare our predictions with the widely used Sheth–Tormen (ST) model. While both models perform similarly at low to intermediate redshifts $0.0 < z < 2.0$, our framework provides a substantially more accurate description at higher redshifts ($z > 2$), particularly for the most massive halos. This contrast becomes increasingly pronounced in the early Universe: at $z = 18.37$, the ST model shows deviations of 70 – 80%, whereas the GPS+ model keeps discrepancies below 20%.

The uniqueness of this study is twofold: first the HMF is measured over an exceptionally wide mass and redshift range using the suite of UCHUU simulations; second, our model is able to predict the HMF over this range more reliably than any other existing formulation.

6. Data Availability

The GPS+ model presented in this work is public in the UCHUU Github repository[†] and will be implemented in COLLOSSUS. The combined HMF measured from the UCHUU simulation suite is provided in electronic tables (see Appendix A). The new MUCHO-UCHUU-140M, MUCHO-UCHUU-1G, and MUCHO-UCHUU-6G simu-

lation products will be made publicly available on the SKIES & UNIVERSES website.

Acknowledgements. We thank Benedikt Diemer for incorporating our HMF model on COLLOSSUS and giving high-valuable comments to this work. EFG acknowledges financial support from the Severo Ochoa grant CEX2021-001131-S funded by MCIN/AEI/ 10.13039/501100011033. EFG and FP acknowledge support from the Spanish MICINN funding grant PGC2018-101931-B-I00. EFG and FP thank Instituto de Astrofísica de Andalucía (IAA-CSIC), Centro de Supercomputación de Galicia (CESGA) and the Spanish academic and research network (RedIRIS) in Spain for hosting Uchuu DR1, DR2 and DR3 in the SKIES & UNIVERSES site for cosmological simulations. TI has been supported by IAAR Research Support Program in Chiba University Japan, MEXT/JSPS KAKENHI (Grant Number JP19KK0344 and JP25H00662), MEXT as “Program for Promoting Researches on the Supercomputer Fugaku” (JPMXP1020230406), and JICFuS. The Uchuu simulations were carried out on Aterui II supercomputer at Center for Computational Astrophysics, CfCA, of National Astronomical Observatory of Japan, and the K computer at the RIKEN Advanced Institute for Computational Science. The Mucho-Uchuu simulations were carried out on the supercomputer Fugaku provided by the RIKEN Center for Computational Science (Project ID: hp240184, and hp250149). The Uchuu Data Releases efforts have made use of the skun@IAA_RedIRIS and skun6@IAA computer facilities managed by the IAA-CSIC in Spain (MICINN EU-Feder grant EQC2018-004366-P).

References

- Behroozi, P. S., Wechsler, R. H., & Wu, H.-Y. 2013a, *ApJ*, 762, 109
 Behroozi, P. S., Wechsler, R. H., Wu, H.-Y., et al. 2013b, *ApJ*, 763, 18
 Betancort-Rijo, J. & López-Corredoira, M. 2000, *ApJ*, 534, L117
 Betancort-Rijo, J. E. & Montero-Dorta, A. D. 2006a, *ApJ*, 653, L77
 Betancort-Rijo, J. E. & Montero-Dorta, A. D. 2006b, *ApJ*, 650, L95
 Betancort-Rijo et al. in prep.
 Bond, J. R., Cole, S., Efstathiou, G., & Kaiser, N. 1991, *ApJ*, 379, 440
 Bryan, G. L. & Norman, M. L. 1998, *ApJ*, 495, 80
 Castro, T., Marra, V., & Quartin, M. 2016, *MNRAS*, 463, 1666
 Cooray, A. & Sheth, R. 2002, *Phys. Rep.*, 372, 1
 DESI Collaboration. 2025, arXiv e-prints, arXiv:2503.14745
 Despali, G., Giocoli, C., Angulo, R. E., et al. 2016, *MNRAS*, 456, 2486
 Diemer, B. 2018, *ApJS*, 239, 35
 Ghirardini, V., Bulbul, E., Artis, E., et al. 2024, *A&A*, 689, A298
 Ishiyama, T., Fukushima, T., & Makino, J. 2009, *Publications of the Astronomical Society of Japan*, 61, 1319
 Ishiyama, T., Nitadori, K., & Makino, J. 2012, arXiv e-prints, arXiv:1211.4406
 Ishiyama, T., Prada, F., Klypin, A. A., et al. 2021, *MNRAS*, 506, 4210
 Ishiyama et al. in prep.
 Ivezić, Ž., Kahn, S. M., Tyson, J. A., et al. 2019, *ApJ*, 873, 111
 Jenkins, A., Frenk, C. S., White, S. D. M., et al. 2001, *MNRAS*, 321, 372
 Kashibadze, O. G., Karachentsev, I. D., & Karachentseva, V. E. 2020, *A&A*, 635, A135
 Lacey, C. & Cole, S. 1993, *MNRAS*, 262, 627
 Laureijs, R., Amiaux, J., Arduini, S., et al. 2011, arXiv e-prints, arXiv:1110.3193
 McElwain, M. W., Feinberg, L. D., Perrin, M. D., et al. 2023, *PASP*, 135, 058001
 Mo, H., van den Bosch, F. C., & White, S. 2010, *Galaxy Formation and Evolution*
 Montero-Dorta, A. D. & Betancort-Rijo, J. 2006, university of La Laguna, Tenerife, Spain
 Planck Collaboration. 2016, *A&A*, 594, A13
 Planck Collaboration. 2020, *A&A*, 641, A6
 Press, W. H. & Schechter, P. 1974, *ApJ*, 187, 425
 Reed, D., Gardner, J., Quinn, T., et al. 2003, *MNRAS*, 346, 565
 Sánchez-Conde, M. A., Betancort-Rijo, J., & Prada, F. 2007, *MNRAS*, 378, 339
 Seppi, R., Comparat, J., Nandra, K., et al. 2021, *A&A*, 652, A155
 Sheth, R. K., Mo, H. J., & Tormen, G. 2001, *MNRAS*, 323, 1
 Sheth, R. K. & Tormen, G. 1999, *MNRAS*, 308, 119
 Shirasaki, M., Ishiyama, T., & Ando, S. 2021, *ApJ*, 922, 89
 Takada et al., M. 2014, *PASJ*, 66, 1
 Tinker, J., Kravtsov, A. V., Klypin, A., et al. 2008, *ApJ*, 688, 709
 Tokue, T., Ishiyama, T., Osato, K., Tanaka, S., & Behroozi, P. 2024, arXiv e-prints, arXiv:2412.18629

[†]<https://github.com/uchuuproject/>

Appendix A: Halo mass function from simulations

Table A.1 provides an example of the release HMF data, corresponding to redshift $z = 0$. This table, along with 19 additional ones (20 in total, with redshifts listed in Table A.2), will be made available electronically at the CDS. Each table includes the following columns: M_{200m} , $f(M)$, $\Delta f(M)$, #halos, Simulation, where M_{200m} is the mass enclosed within overdensity $200\rho_b$; $f(M)$ is the multiplicity function (Equation 1); $\Delta f(m)$ is its associated uncertainty; the number of halos corresponds to the count in each mass bin, #; and the simulation name indicates which simulation contributed the HMF measurement for that bin.

Table A.1: HMF at $z = 0.0$ from different cosmological simulations. Columns list: M_{200m} , the halo mass within overdensity $200\rho_b$; $f(M)$, the mass function; $\Delta f(M)$, its uncertainty; the number of halos in each mass bin; and the name the name of the simulation contributing that bin. Only the first and last bins for each simulation are shown; ellipses indicate omitted intermediate values. Complete tables for all redshifts used in Fig. 1 are available in electronic form.

$M_{200b} [M_\odot/h]$	$f(M)$	$\Delta f(M)$	#halos	Simulation
4.9×10^6	1.80×10^{-1}	3.5×10^{-4}	2.6×10^5	Phi-4096
...	"
2.7×10^8	2.23×10^{-1}	2.7×10^{-3}	7.1×10^3	Phi-4096
3.7×10^8	2.21×10^{-1}	1.2×10^{-4}	3.6×10^6	Shin-Uchuu
...	"
8.7×10^{10}	2.93×10^{-1}	1.7×10^{-3}	2.8×10^4	Shin-Uchuu
1.2×10^{11}	2.98×10^{-1}	2.8×10^{-3}	4.8×10^5	MU-140M
...	"
4.9×10^{11}	3.27×10^{-1}	5.4×10^{-3}	1.4×10^5	MU-140M
6.5×10^{11}	3.25×10^{-1}	2.8×10^{-4}	7.6×10^7	MU-1G
...	"
2.7×10^{13}	3.33×10^{-1}	1.5×10^{-3}	2.5×10^6	MU-1G
3.7×10^{13}	3.23×10^{-1}	1.4×10^{-4}	4.0×10^8	MU-6G
...	"
4.9×10^{15}	1.07×10^{-4}	1.7×10^{-5}	1.6×10^3	MU-6G

z	Phi-4096	Shin-Uchuu	Uchuu	MU-140M	MU-1G	MU-6G
0.00	Y	Y	Y	Y	Y	Y
0.49	Y	Y	Y	Y	-	-
1.03	Y	Y	Y	Y	Y	Y
2.03	Y	Y	Y	Y	Y	Y
2.95	-	Y	Y	Y	Y	Y
4.27	Y	Y	Y	Y	Y	-
5.15	-	Y	Y	Y	Y	-
6.34	-	Y	Y	Y	Y	-
7.03	-	Y	Y	Y	Y	-
8.58	Y	Y	Y	Y	Y	-
9.47	Y	Y	Y	Y	Y	-
10.44	Y	Y	Y	Y	Y	-
11.50	Y	Y	Y	Y	Y	-
12.66	Y	Y	Y	Y	Y	-
13.93	Y	Y	Y	Y	-	-
14.32	Y	Y	-	-	-	-
15.57	Y	Y	-	-	-	-
16.92	Y	Y	-	-	-	-
18.37	Y	Y	-	-	-	-
19.95	Y	Y	-	-	-	-

Table A.2: Availability of simulation snapshots at each redshift for the different simulations. 'Y' indicates that a snapshot exists at the corresponding redshift, and '-' indicates that no snapshot is available for that simulation. MU denotes the MUCHO-UCHUU simulations.

Appendix B: Basic considerations about the theoretical framework

The PS formalism yields a halo mass fraction $F(M)$ that is not correctly normalized ($F(M = 0) = \frac{1}{2}$, instead of one). Furthermore, it predicts a high-mass tail that is too steep. This is rather puzzling because, while in other mass ranges there is ample room for improving the theoretical treatment, in this limit the spherical collapse approximation used in the PS formalism should become asymptotically exact. This is due to a selection effect: only protohaloes undergoing an almost perfectly spherical collapse have any chance of having formed by the time being considered.

ST combined ellipsoidal collapse with the PS approach and obtained a substantial improvement in the low-mass regime, but they did not solve either the high-mass problem or the normalization issue.

In Betancort-Rijo & Montero-Dorta (2006b), it was pointed out that the origin of these two problems lies in the PS assumptions themselves. The criterion used by those authors to decide whether a mass element belongs to an object with mass larger than M was that a sphere with Lagrangian radius $r(M)$, centred on that element, satisfies the condition for spherical collapse (i.e. the linear fractional mass density fluctuation within the sphere, δ_l , obeys $\geq \delta_c$). This criterion cannot be exact, since not all mass elements can be located at the centres of the objects that contain them.

We adopted a more realistic and less restrictive criterion: a mass element belongs to a halo of mass M if it lies within a distance $r(M)$ of a point that satisfies the collapse condition described above. This formulation allows an analytical treatment, leading to the mass fraction $F(m)$ expression in Equation 3, where $V(\Sigma, m)/2$ represents the ratio between the probability that $\delta_l \geq 1.686$ within a sphere with radius $r(M)$ centered on a randomly selected mass element and the greater probability that such an element belongs to an object with mass larger than M . In that work, we used the spherical collapse approximation, so that $< \delta_c > (\sigma, M) = \delta_c$ is constant (taken as either 1.686, or, 1.676). Under this formulation, both the high-mass limit and the normalization behave correctly.

In Montero-Dorta & Betancort-Rijo (2006), we used the Complete Zel'dovich Approximation (CZA) (Betancort-Rijo & López-Corredoira 2000), which effectively corresponds to ellipsoidal collapse, to compute the mean value of δ_l within the region (generally ellipsoidal) that collapses into an object of mass M . We denoted this mean value by $< \delta_l >$, and its variance by U^2 . Both quantities were found to depend on M and z only through $\sigma(M, z)$, to a very good approximation). In the present work, the variance obtained in that study has been fitted using the expression given in Equation 6. For $< \delta_l >$, the result obtained in that work was:

$$< \delta_l > = \delta_c \left[0.814 + 0.688 \left(\frac{\sigma}{\delta_c} \right) - 0.033 \left(\frac{\sigma}{\delta_c} \right)^2 + 0.02 \left(\frac{\sigma}{\delta_c} \right)^3 \right] \quad (\text{B.1})$$

This expression corresponds to the first factor in Equation 7. The second factor introduces a small explicit dependence on M whose origin and derivation will be presented in Betancort-Rijo et al. (in prep.).

Equation B.1 was obtained using a model for shell-crossing and stabilization in which the protohalo, upon collapsing along one direction in comoving coordinates to $\frac{1}{13}$ of its original size,

becomes stabilized along that axis while continuing to collapse along the remaining directions.

This stabilization model is physically well motivated but not exact, so we introduced the parameters A and B , which are expected to remain close to unity, to account for its approximations.

It is important to note that in this formalism $F(M)$ depends on mass not only through $\sigma(M, z)$, but also through an explicit dependence on M that reflects the shape of the power spectrum at that scale M . This dependence appears in Equation 7 through $b(M)$ (8) and in $V(M)$ (Equation 4) through $c(M)$ (Equation 9).

It should also be emphasized that there is no explicit dependence on redshift, and that $F(M)$ is correctly normalized without requiring parameters fitting. The only fitted parameters are A and B in $\langle \delta_c \rangle (\sigma, M)$, which, based on theoretical considerations, are expected to remain close to unity. In principle, their values could be determined directly from simulations by analysing the behaviour of this function, since analytically we cannot extend the derivation beyond B.1.

Appendix C: Dependence of the HMF with the halo mass definition

As part of this work, we assessed the impact of different halo mass definitions in our theoretical framework. The HMF results presented in Section 4 are based on the M_{200m} mass definition; however, the virial mass, M_{vir} , can also be adopted. Figure C.1 compares the performance of the model under both definitions. The largest differences arise at low redshift. When using the virial mass, the agreement at the high-mass end worsens significantly, with ratios dropping to ~ 0.5 , corresponding to discrepancies of $\sim 50\%$ between the model predictions and the measured HMFs from the simulations. At higher redshifts, the performance of the model using the virial mass becomes comparable to that obtained using the M_{200m} definition.

This analysis shows that the choice of halo mass definition has a strong impact on the performance of the model, particularly at low redshifts, where the difference between M_{vir} and M_{200m} becomes significant. The virial mass definition does not appear to be suitable in this context, as no choice of fitted parameters yields a good agreement at the high-mass end of the HMF at $z = 0.0$. This behaviour is related to the fact that the virial overdensity, Δ_{vir} , is not constant. In the UCHUU simulation suite, Δ_{vir} evolves following Bryan & Norman (1998), giving $\Delta_{vir}(z = 0) \approx 102$, $\Delta_{vir}(z = 1.03) \approx 159$, and approaching the Einstein–de Sitter value of 178 at higher redshift. That work argues that the density contrast at virialization should depend on Ω_m (and thus on redshift for Λ CDM cosmologies). However, there are strong counterarguments suggesting that Δ_{vir} should be nearly independent of redshift. A detailed discussion of this point and its theoretical implications will be presented in Betancort-Rijo et al. (in prep.); here, we simply highlight that the available evidence points toward a weak or negligible redshift dependence of Δ_{vir} .

In Sánchez-Conde et al. (2007), we investigated the spherical collapse model with shell-crossing to study the stabilization of proto-haloes. No difference was found between Einstein–de Sitter and Λ CDM cosmologies.

If the results of Bryan & Norman (1998) were correct and the stabilization process truly depended on redshift, then the HMF constructed using M_{200m} should exhibit explicit redshift dependence. In that case, the formalism presented here - which contains no explicit dependence on z - would be unable to reproduce the simulation results accurately. Conversely, the HMF

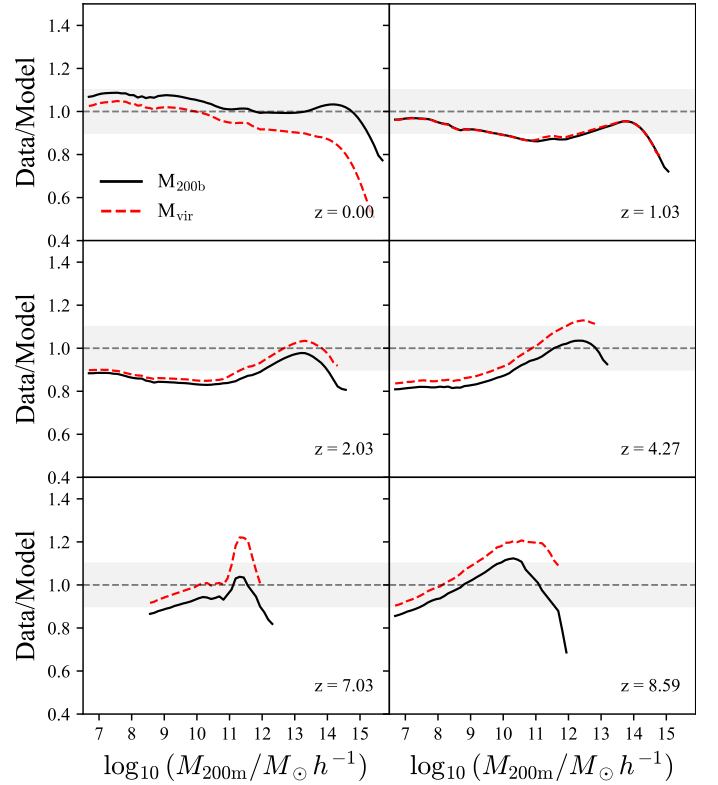


Fig. C.1: Comparison of the ratio between the simulated HMF and the GPS+ model at different redshifts, for two halo mass definitions in the data: the mass enclosed within overdensity $200\rho_b$, M_{200m} , and the mass within the virial radius, M_{vir} .

constructed using M_{vir} , together with its redshift-dependent Δ_{vir} , would account for the assumed redshift dependence of the stabilization process and thus eliminate this source of spurious explicit redshift dependence. Under such circumstances, the HMF based on M_{vir} would be expected to appear more universal.

However, Figure C.1 shows the opposite behavior: the HMF constructed using M_{200m} provides a significantly better match to the formalism (which is explicitly independent of z), and therefore yields a more universal HMF.

It should be noted that in Figure C.1, the M_{vir} data from the simulations are compared with the predictions of the formalism using parameter values slightly adjusted relative to those employed for M_{200m} , in order to obtain the best possible agreement across the full redshift range. Even with this optimization, the model fails to accurately reproduce the HMF at low redshift when using M_{vir} at $z = 0$, there is a pronounced discrepancy for high-mass end, while for $z = 1.03$ and larger z 's the difference residues for both mass definitions are within the accuracy of the formalism. Since for these redshifts Δ_{vir} changes little according to Bryan & Norman (1998) formalism, this support the conclusion that Δ_{vir} is in fact almost independent of redshift.